Journal of Magnetic Resonance 338 (2022) 107197

Contents lists available at ScienceDirect

Journal of Magnetic Resonance

journal homepage: www.elsevier.com/locate/jmr

How to improve the efficiency of a traditional dissolution dynamic nuclear polarization (dDNP) apparatus: Design and performance of a fluid path compatible dDNP/LOD-ESR probe

Thanh Phong Lê [a,b], Jean-Noël Hyacinthe [a,c], Andrea Capozzi [b,d,*]

[a] Geneva School of Health Sciences, HES-SO University of Applied Sciences and Arts Western Switzerland, Avenue de Champel 47, 1206 Geneva, Switzerland
[b] LIFMET, Institute of Physics, École polytechnique fédérale de Lausanne (EPFL), Station 6, 1015 Lausanne, Switzerland
[c] Image Guided Interventions Laboratory, Department of Radiology and Medical Informatics, University of Geneva, Rue Gabrielle–Perret–Gentil 4, 1211 Geneva, Switzerland
[d] HYPERMAG, Department of Health Technology, Technical University of Denmark, Building 349, 2800 Kgs Lyngby, Denmark

ARTICLE INFO

Article history:
Received 22 January 2022
Revised 12 March 2022
Accepted 14 March 2022
Available online 16 March 2022

Keywords:
Hyperpolarization
dDNP
Fluid path
LOD-ESR
Heat conduction at cryogenic temperatures

ABSTRACT

Dissolution Dynamic Nuclear Polarization (dDNP) was invented almost twenty years ago. Ever since, hardware advancement has observed 2 trends: the quest for DNP at higher field and, more recently, the development of cryogen free polarizers. Despite the DNP community is slowly migrating towards "dry" systems, many "wet" polarizers are still in use. Traditional DNP polarizers can use up to 100 L of liquid helium per week, but are less sensitive to air contamination and have higher cooling power. These two characteristics make them very versatile when it comes to new methods development.

In this study we retrofitted a 5 T/1.15 K "wet" DNP polarizer with the aim of improving cryogenic and DNP performance. We designed, built, and tested a new DNP insert that is compatible with the fluid path (FP) technology and a LOgitudinal Detected Electron Spin Resonance (LOD-ESR) probe to investigate radical properties at real DNP conditions. The new hardware increased the maximum achievable polarization and the polarization rate constant of a [1-^{13}C]pyruvic acid-trityl sample by a factor 1.5. Moreover, the increased liquid He holding time together with the possibility to constantly keep the sample space at low pressure upon sample loading and dissolution allowed us to save about 20 L of liquid He per week.

1. Introduction

In recent years, hyperpolarized Magnetic Resonance (MR) has become a well-established branch of MR thanks to the unprecedented sensitivity gain it can give access to [1–11].

Among the different hyperpolarization techniques targeting the liquid state, dissolution Dynamic Nuclear Polarization (dDNP) is probably the one requiring the most expensive and technically demanding hardware [12]. Invented in 2003 by Ardenkjaer-Larsen and co-workers [13], dDNP produces solutions of hyperpolarized nuclei by suddenly dissolving solid frozen samples prepared by DNP [14]. Being the polarization transferred to the nuclei of interest from unpaired electron spins via microwave irradiation, operating at low temperatures (1–1.5 K) and high magnetic field (3.35 – 7 T) [15–17] is a key requirement for this technique. Indeed, the electrons' Boltzmann polarization sets the theoretical limit that the nuclear spins can achieve.

These experimental conditions are provided by the so-called "dDNP polarizer". In its most general definition, a dDNP polarizer is a cold-bore magnet equipped with a source/waveguide apparatus able to shine microwaves at the appropriate frequency onto the magnet isocenter, and a dissolution system that instantly melts and extracts the hyperpolarized sample. Most importantly, liquid He is used to cool the sample down to the target temperature. Traditional dDNP polarizers [15,18,19], based on a "wet-cryostat" design needing the provision of liquid He from an external source, can use up to 100 L of the cryogenic fluid per week. Liquid He is a non-renewable expensive commodity, and not all facilities are equipped with recovery systems. Therefore, the dDNP community, inspired by the clinical and commercially available SPINlab (GE Heathcare, Chicago Illinois, USA) [20], is progressively moving towards cryogen-free systems able to recondense the boiled off He gas in a closed loop by using a cryocooler [21–23]. These systems are excellent "workhorses" for application experiments and have the clear advantage of low running costs and absence of cryo-

* Corresponding author at: EPFL SB IPHYS LIFMET, CH F1 633 (Bâtiment CH), Station 6, CH-1015 Lausanne, Switzerland.
E-mail address: andrea.capozzi@epfl.ch (A. Capozzi).

https://doi.org/10.1016/j.jmr.2022.107197
1090-7807/

genics to handle. Moreover, they are often equipped with a dissolution apparatus based on the fluid path (FP) technology to minimize the heat load during the process [20,21,23]. Indeed, the FP allows to efficiently melt the hyperpolarized sample without repressurizing the sample space and having to introduce an external dissolution wand.

Nevertheless, cryogen-free systems have three main disadvantages: a high upfront investment, a limited cooling power (few Watts), a higher sensitivity to air contamination.

On the other hand, "wet cryostat"-based dDNP polarizers are still used on a daily basis by several groups [24–27]. These systems, being more robust and offering higher cooling power, are very flexible and versatile when it comes to methods developments. The old generation of dDNP polarizers was designed between 10 and 20 years ago [13,19]. Ever since, no real improvement has been provided.

In this study, with the purpose of improving the cryogenic and polarization performance of an existing wet 5 T/1.15 K DNP polarizer [18], we detail the cost-effective implementation of a new DNP probe compatible with a custom fluid path system (CFP) [12,24,28,29]. Furthermore, we show how the new design allows to easily complement the apparatus with a home-built LOD-ESR spectrometer with the purpose of investigating the radical properties at real DNP experimental conditions [29,30].

2. Materials and methods

2.1. Original setup

The DNP polarizer being upgraded (Vanderklink Sarl, La Tour-de-Peilz, Switzerland) is similar for design and working principle to the prototype developed by Comment et al. in 2007 [18]. It is based on a vertical unshielded 89 mm wide bore magnet (Bruker Spectrospin, Fällanden, Switzerland) set to a field strength of 5 T corresponding to an ESR frequency of about 140 GHz. The magnet bore accommodates a double-walled 316L stainless-steel cryostat equipped with two copper radiation shields and a tail section of 50/80 mm ID/OD (Leiden Cryogenics B.V., Kenauweg 11, 2331 BA Leiden, Netherlands). The cryostat inner vacuum chamber (IVC) hosts the variable temperature insert (VTI) to condense and control the helium flow. The latter mounts, at the top of the tail, a 316L stainless-steel gas/liquid He phase separator used to refill, with minimal perturbation, the 36.5 mm wide sample space.

Although the cryostat is of the continuous flow type, it is generally operated in batch mode to achieve lower temperature. Firstly, it is filled with liquid helium from an external dewar via a rigid transfer line ending inside the phase separator. Then, the phase separator is isolated from the sample space by closing two needle valves, and the He bath is pumped on by a 253 m^3/h root pump (Ruvac WAU 251, Leybold, Cologne, Germany) backed by a 65 m^3/h rotatory pump (Trivac D65B, Leybold). This procedure enables to reach a helium bath temperature of (1.15 ± 0.05) K.

Two peculiarities characterize the original dDNP polarizer design by Comment et al. [18]: insertion and dissolution of the sample happen at atmospheric pressure, and the waveguide has to be removed upon insertion of the dissolution wand.

Supplementary Figure S1 shows all parts of the original design that have been replaced in this study: the "DNP insert" (or main insert) including the brass microwave cavity, the NMR coil with its stainless steel outer conductor coaxial cable, the brass baffles to cut thermal convection and radiation; the fiber glass "sample stick" for sample insertion into the polarizer; the gold-plated stainless steel "removable waveguide", slid inside the sample stick, carrying the microwaves onto the sample space; the carbon fiber dissolution wand to be inserted instead of the waveguide to instantly transform the solid frozen sample into an injectable hyperpolarized solution.

2.2. CFP compatible DNP insert

The CFP presented previously [12,23,24,28,29] has been adapted to the length of the retrofitted polarizer (Fig. 1, the different components are reported in bold italic in the text). The red arrow pointing down indicates the input for the superheated buffer; the green arrow pointing right indicates the output for the hyperpolarized solution. The superheated buffer reaches the sample flowing through a 1/16″ natural color PEEK inner capillary - not shown- (Zeus Inc., Orangeburg, NC, USA); the hyperpolarized solution is ejected from the polarizer flowing in between the 1/16″ inner capillary and a 1/8″ black color PEEK outer capillary (***D***, Zeus Inc., Orangeburg, NC, USA). The stainless steel "quick connect" (***A***, SS-QM2-B-200, Swagelok, Solon, OH, USA) allows coupling of the CFP to the "dissolution head" boiler (see Supplementary Figure S2). The PEEK "flow separator" (***B***, P-713, IDEX Health & Science, Lake Forest, IL, USA) splits the dissolution buffer from the hyperpolarized solution. The home-built PEEK (***C***, Ketron 1000, Mitsubishi Chemical Advanced Materials, Tielt, Belgium) "dynamic sealing" allows to move the sample vial inside the polarizer downwards for insertion and upwards for dissolution/extraction while keeping the sample space at low pressure. The home-built vial is reusable and made of a PEEK "vial top-part" (***E, Ketron 1000, Mitsubishi Chemical Advanced Materials***), laser welded (Leister Technologies, Kaegiswil, Switzerland) to the outer capillary, and a PAI "vial bottom-part" (***F, Duratron T4203, Mitsubishi Chemical Advanced Materials***) containing the sample (500 μL of maximum capacity). The two parts are made leak tight to superfluid He by compressing a PTFE o-ring (Kremer GmbH, Wächtersbach, Germany) to be replaced before each new loading. The "one-way valve" (***G***, AKH04-00, SMC, Tokyo, Japan) at the outlet prevents air cryo-pumping when the vial is at low temperature inside the polarizer. A detailed description of the assembling procedure and functioning principle of the CFP was provided in the work by Capozzi et al. [24].

A new DNP insert was designed to accommodate the CFP into the polarizer (Fig. 2, the different components are reported in bold italic in the text).

The insert is built around a 1320 mm long 316L stainless steel 12.0/13.0 mm ID/OD tube (***B***, Interalloy AG, Schinznach-Bad, Switzerland) inside which the CFP slides to reach the magnet isocenter. An "air lock compartment", composed of a vial 316L stainless steel "loading chamber" (***G***) and a KF 16 gate valve (***H***, Vatlock 01224-KA06, VAT, Haag, Switzerland), is attached to the top of the sample tube as a buffer volume between the room and the low-pressure sample space.

A home-built 316L stainless steel KF 40 flange seals the insert to the VTI and provides hermetic RF (***C***, feedthrough SMA connector, SF-2991-6002, Amphenol SV Microwave, West Palm Beach, USA) and microwave (***A***, circular 4.6 mm to rectangular WR-06 transition, Elmika, Vilnius, Lithuania) interfaces. Polished brass baffles (***I***) are brazed along the stainless-steel tube to reduce thermal convection and radiation and to provide mechanical support to the 4.6/5.0 mm ID/OD circular 316L stainless-steel waveguide (***E***, Interalloy AG, Schinznach-Bad, Switzerland) and the semi-rigid coaxial cable with stainless steel outer conductor (***D***,.141SS-W-P-50, Jyebao, Taiwan). The waveguide is interfaced to the microwave source (VCOM-06/140/1/50-DD, ELVA-1, Tallinn, Estonia) with a 90° WR-06 E-plane bend (Elmika, Vilnius, Lithuania).

The 13.2 cm^3 copper cavity (***F***) is polished to reduce microwave absorption. The cavity wall is angled at 45° at the waveguide output to reflect the microwaves onto the DNP sample. A copper Alderman-Grant coil (***J***, 8 mm ID 16 mm window height) supported

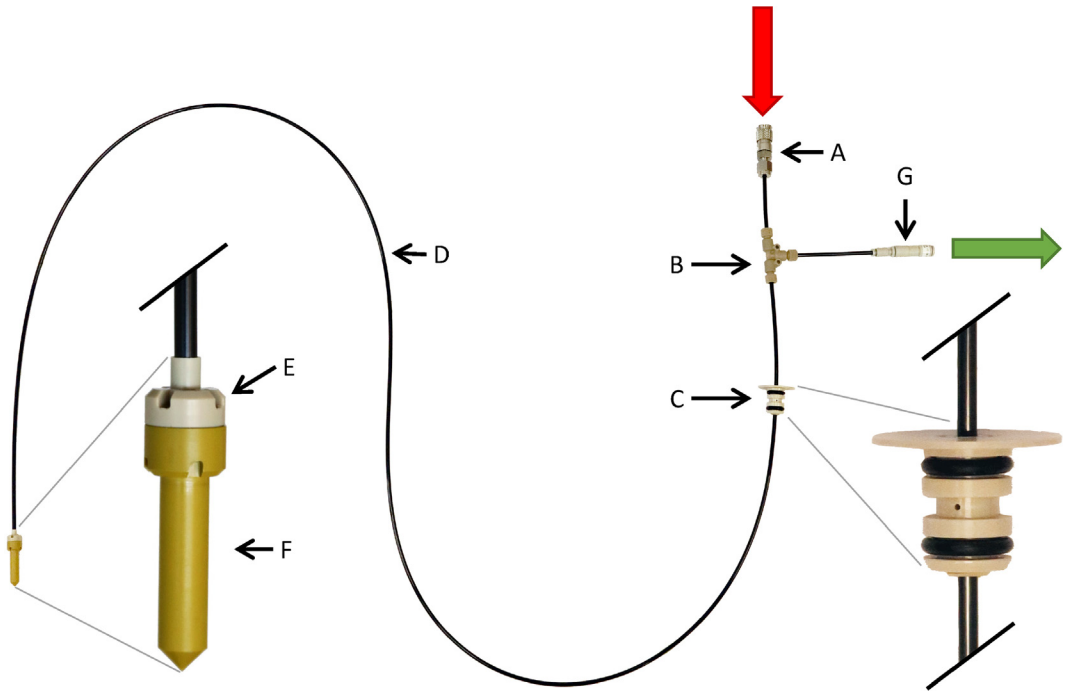

Fig. 1. The figure shows the Custom Fluid Path (CFP) used in this study. The device is composed by a "quick connect" (**A**); a "flow separator" (**B**); a "dynamic sealing" (**C**); "coaxial capillaries" (**D**), whose only the outer 1/8" one is shown; a "vial top-part" (**E**), a "vial bottom-part" (**F**) and a "one-way valve" (**G**). To adapt the CFP to this polarizer the coaxial capillary length was increased to 1500 mm with respect to the original study [24]. The red and green arrows indicate the inlet and outlet, respectively. (For interpretation of the references to color in this figure legend, the reader is referred to the web version of this article.)

by a PTFE coil former (not shown), is inserted into the cavity for solid-state NMR detection. The coil is remotely tuned and matched outside of the cryostat with a coaxial cable and a matching network with two piston trimmer capacitors (Voltronics V1949).

A dedicated "CFP pressure-test station" (Supplementary figure S3) was built to provide pressurized helium for leak-testing [20,29], and compressed air for drying the CFP after dissolution. Loading of the CFP inside the polarizer is similar to what was earlier described [24,29]: the CFP is first connected to the pressure-test station He gas stem, and the pressure regulator set to provide a tiny flow; after pipetting the liquid sample inside the bottom part of the vial and connecting it to the top part, the vial is immersed in liquid nitrogen to flash-freeze the sample solution; the CFP output is closed with a stopcock valve, the He gas pressure inside the CFP increased to 4 bar, and the CFP inlet closed. If after 5 min the pressure gauge indicator steadily shows 4 bar, the CFP is considered ready for loading inside the polarizer. At this point, the dynamic sealing is moved down to touch the vial, a mild flow applied to the He gas port (***G1***), and the vial moved inside the loading chamber that is then closed at the top with the dynamic sealing. Finally, the He gas stream is closed, the gate valve opened, and the vial pushed down to reach the NMR coil at the bottom of the DNP insert. During all these operations, the sample space is already cold and continuously pumped, with its pressure that increases from 1 mbar to 10 mbar, at the most.

2.3. LOD-ESR setup

To measure the radical properties at DNP conditions, LOngitudinal Detected (LOD)-ESR was implemented similarly to previous works [29,30].

The LOD-ESR probe (Fig. 3, the different components are reported in bold italic in the text) is built around a CFP outer capillary (***B***) and a dynamic sealing (***C***) such that a similar loading procedure of the sample inside the polarizer can be followed (no leak test needed in this case). The detection coil is a 600-turn copper wire split solenoid made of 0.1 mm enameled copper wire wound around a PEEK (***Ketron 1000, Mitsubishi Chemical Advanced Materials***) coil former (***E***). A 3 mm gap allows the microwaves to reach the sample (cut-off dimension at 140 GHz is 1 mm). The bottom portion of the coil former has an outer diameter of 7.5 mm, small enough to enter the NMR coil of the DNP insert. Up to 120 μL of sample can be loaded into the sample cup (***F***). The latter slides and locks inside the coil former. The coil former is permanently screwed to the vial top part (***D***). The two ends of the detection coil are routed inside the coil former and soldered to a twisted pair of silver-plated copper wires that runs upwards through the black capillary to carry the signal out of the polarizer. Electrical connections are provided at the outer end of the probe (***A***).

The signal is measured using a three stages 106 dB gain differential amplifier (Supplementary figure S4) and NI USB-6002 (National Instruments, Austin, USA) digital acquisition card. To reduce noise pickup, signals are transmitted as a differential pair using BNC Twinax cables between the probe, differential amplifier and acquisition card. Furthermore, all ground loops in the LOD-ESR setup were eliminated: the acquisition card is grounded to the cryostat, powered using a floating DC source, and galvanically separated from the computer using a USB digital insulator (ADuM4160, Analog Devices, Norwood, USA). A voltage controlled variable attenuator (VCVA-06 and ADL-10/100, ELVA-1, Tallinn, Estonia) is added to the output of the microwave source to allow modulation of the output power at a specific frequency to feed the digital lock-in [29].

For electron T_1 (T_{1e}) measurements the output power was modulated at 0.1 Hz between 0 mW and 35 mW. The rate was low enough to record the full time evolution of the electron spins during saturation and relaxation [29]; the signal was averaged 256 times. Extraction of the T_{1e} was performed by fitting the relaxation curve data to the equation representing the signal S evolution as a function of time t: $S(t) = A\left(exp\left(-\frac{t}{T_{1e}}\right) - exp\left(-\frac{t}{\tau}\right)\right)$; where A is a

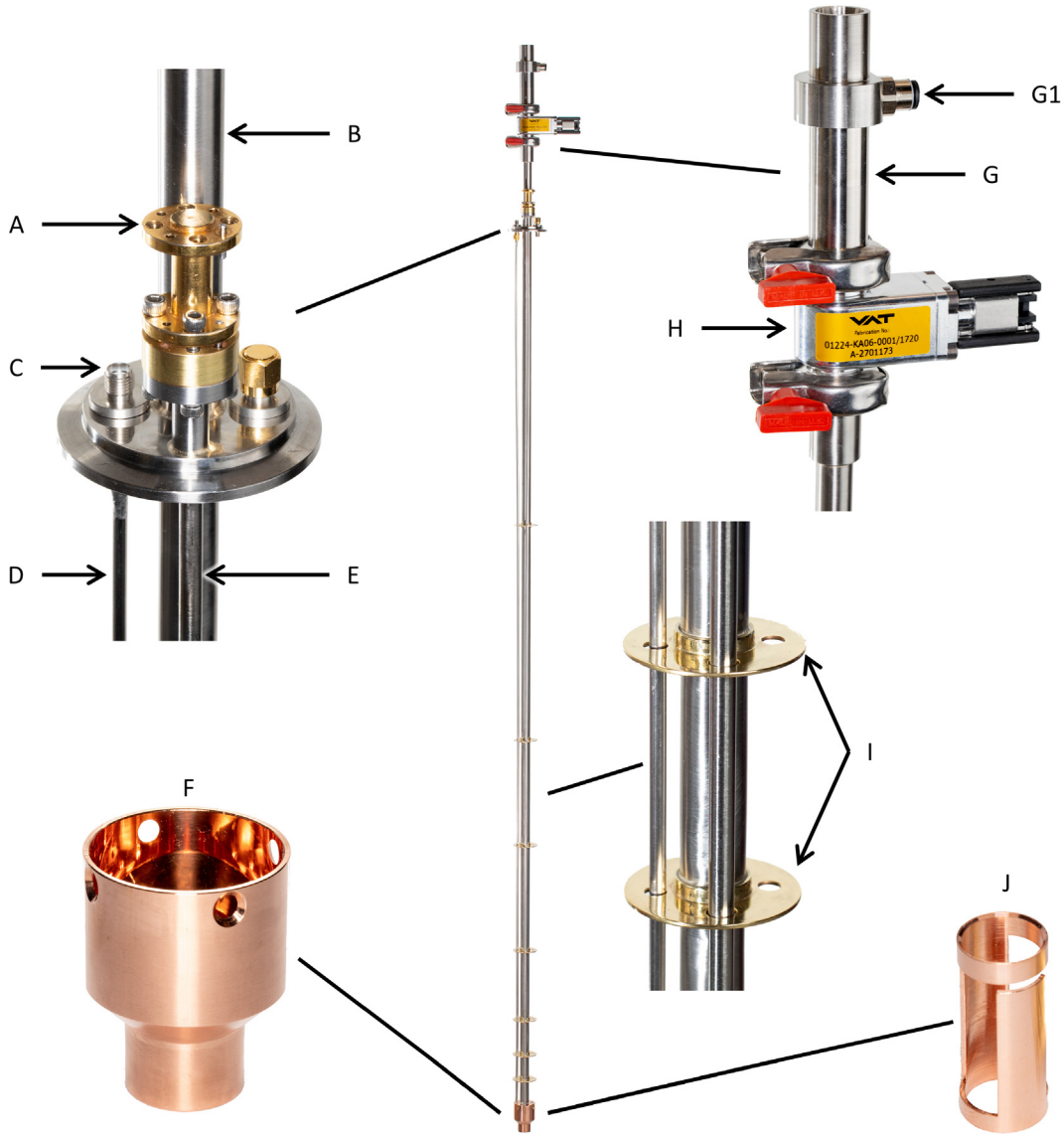

Fig. 2. The figure shows the new DNP insert. The most important parts are zoomed in (follow straight black lines) to better picture the main components: rectangular WR-06 to circular 4.6 mm microwave transition (**A**); stainless-steel sample loading tube (**B**); feedthrough SMA connector (**C**); rigid coax cable (**D**); stainless-steel waveguide (**E**); copper microwave cavity (**F**); loading chamber (**G**) with He gas port (**G1**); gate valve (**H**); brass baffles (**I**), Alderman-Grant copper coil (**J**).

free parameter that represents the highest signal intensity, and τ is the characteristic time constant of the probe. The latter measured 20.6 ms, upon excitation of the set-up with a squared wave [29]. For radical spectrum recording, the microwave frequency was increased from 139.8 GHz to 140.0 GHz in steps of 1.25 MHz and the output power modulated at 4.8 Hz between 0 mW and 35 mW. For each frequency step the demodulated signal was integrated for 20 s in the time domain, equivalent to set the low pass filter of the lock-in to 0.05 Hz.

2.4. Estimation of cryogenic performance

To compare the cryogenic performance of the two DNP inserts, the liquid helium hold time was measured at routinely used DNP conditions, i.e. sample space cooled down to 1.15 K with a sample inside subjected to microwave irradiation. Before each measurement, the polarizer was operated for at least half a day to cooldown the radiation shields of the cryostat below 150 K. Then, a DNP sample was inserted, the helium was filled to the maximum capacity of the polarizer (550 mm above the sample location, approx. 1300 mL of usable liquid helium). The hold-time measurement started, after filling liquid He, once the vacuum pumps lowered the temperature in the sample space below 1.16 K and the microwave irradiation was started at full power (60 mW). The measurement was considered concluded when the temperature into the sample space suddenly dropped below 1.12 K, indication of no residual liquid He inside the sample space. The temperature sensor used was a ruthenium oxide (RuO_2) resistor (10 kΩ at room temperature, RX-103A, Lake Shore Cryotronics, OH-43081, Westerville, USA). Using the same strategy, the holding time measurements for the two inserts were repeated at 4.2 K, keeping the sample space at atmospheric pressure.

2.5. A simple thermal model for heat conduction

We built a simple model for heat conduction only, to help interpreting the cryogenic performance data. The thermal conductivity k (unit $W \cdot m^{-1} \cdot K^{-1}$) relates to the facility with which heat can diffuse into a material. The Fourier's law, in its most general form,

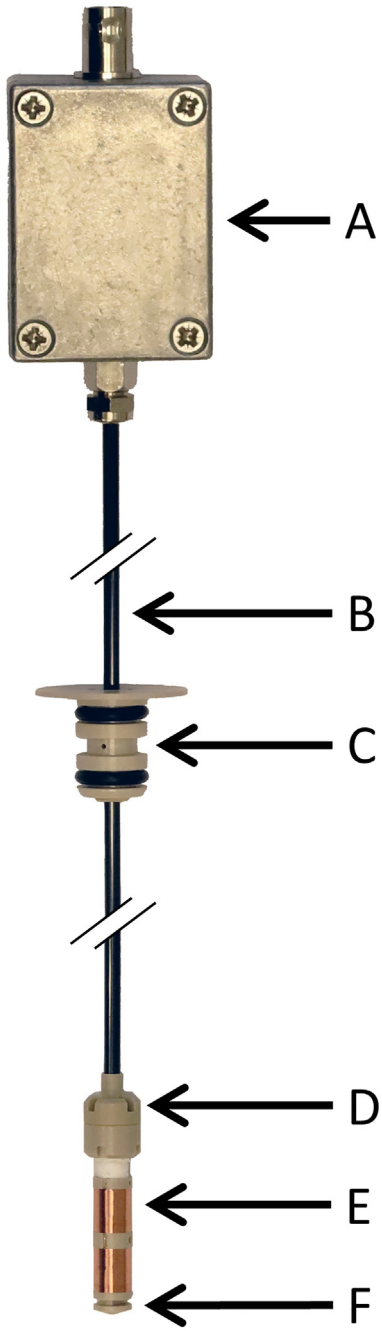

Fig. 3. We report here the LOD-ESR probe designed for this study and compatible with the DNP insert with no need for any modification of the NMR part. The probe is composed by the following elements: a leak-tight connection box that transforms the twisted pair carrying the signal to BNC Twinax connector (**A**); a CFP 1/8″ outer capillary (**B**) with its dynamic sealing (**C**) and laser welded vial top-part (**D**); a coil former supporting a 600-turn spit solenoid (**E**); a sample cup (**F**).

yields the quantity of heat diffusing through a unit surface during a unit of time $d\vec{q}/dt$ within a material subjected to a temperature gradient $\overrightarrow{\nabla T}$ [31]:

$$\frac{d\vec{q}}{dt} = -k\overrightarrow{\nabla T} \tag{1}$$

If the cross section A of the material is constant across its length L, then the problem can be simplified to 1-dimension, and the heat flowing across 2 surfaces distant dx per unit time writes.

$$\frac{dQ}{dt}dx = -Ak\frac{dT}{dx} \tag{2}$$

With $dQ/dt = Adq/dt$. Considering that the thermal conductivity can be temperature dependent and that the ends temperatures, T_{high} and T_{low} are constant, we finally obtain the expression for the power transmitted across the material:

$$\frac{dQ}{dt} = -\frac{A}{L}\int_{T_{high}}^{T_{low}} k(T)dT \tag{3}$$

To evaluate the difference in heat conduction between the two DNP inserts, equation (3) was numerically integrated using MATLAB (MathWorks, Natick, Massachusetts, USA). For all calculations, T_{high} and T_{low} were set to 295 K and 1.15 K, respectively; the cross section of each component was calculated according to the geometry (Table 1). The temperature dependent thermal conductivity for the different materials was obtained interpolating data tables from [31] and [32]. Since the transported heat per unit time depends on the length of the conductor, the calculation for each component was ran for 2 values of L: 1200 mm (distance between the cryostat isocenter and the KF40 flange and corresponding to an almost empty cryostat) and 1200–550 mm (corresponding to a full cryostat). The MATLAB code is reported in Supporting Information.

2.6. Sample preparation

For this study, one single kind of sample was used: [1-^{13}C]pyruvic acid (Sigma Aldrich, Buchs, Switzerland) doped with 15 mM of AH111501 trityl radical (Albeda Research, Copenhagen, Denmark). LOD-ESR experiments were performed on 100 μL samples, while DNP on 5 μL samples.

Samples were prepared fresh before each experiment.

2.7. Solid-state DNP measurements

Solid-state DNP performance was investigated for the two inserts in separate experiments. In both cases, 5 μL of sample was loaded inside the sample cup/vial together with NaOH at stoichiometric ratio (7.2 μL of 10 M NaOH in H_2O) to neutralize the pyruvic acid upon dissolution.

A Cameleon 3 NMR spectrometer (RS2D, Mundolsheim, France) was used with both inserts to monitor the solid-state NMR signal.

Firstly, a microwave frequency sweep from 139.8 to 140.0 GHz, in steps of 10 MHz, was performed to measure the DNP spectrum of the sample and determine optimal irradiation condition (n = 1). For each frequency step, the sample was hyperpolarized with 55 mW microwave power and the NMR signal was acquired with a 30° hard pulse after 10 min. Before each polarization interval, microwaves were switched off and the polarization destroyed with 1000 x 10° hard pulses.

Secondly, working at 139.86 GHz, a microwave power sweep was performed to investigate power density differences between the 2 inserts (n = 1). The power was increased from 1 mW to 3 mW in steps of 1 mW, from 5 mW to 60 mW in steps of 5 mW and a final step at 63 mW which is the maximal power output at this frequency.

Finally, at optimal DNP condition (i.e. 55 mW and 139.86 GHz for the new insert, and 63 mW and 139.86 GHz for the old one), the samples were hyperpolarized and monitored with a hard 5° pulse every 120 s to measure the buildup curves (n = 3). The experiments lasted from 3 to 3.5 h, more than three times the build-up time constant (i.e. at least 95% of the polarization plateau, result of a mono-exponential curve fit).

To assess the NMR sensitivity, the signal-to-noise ratio (SNR) in the last 20 min (10 data points) was averaged and normalized to the sample volume.

Table 1
Specifications of the DNP insert components used in the heat conduction simulations.

Component name	Components number	Components material	OD (mm)	ID (mm)	Cross sec. (mm^2)	Heat cond. (mW)	Heat cond. (%)
Mounting rod	3	Steel 316L	3.0	0.0	7.07	52.90	71.6
Wave guide	1	Steel 316L	6.0	5.6	3.64	9.10	12.3
Sample stick	1	Fiber glass	16.0	14.0	47.12	4.30	5.8
Coax cable shield	1	Steel 316L	3.6	3.0	3.11	7.70	10.4
Old insert	**6**	**Miscellaneous**	\	\	\	**73.90**	**100**
Component name	**Component number**	**Component material**	**OD (mm)**	**ID (mm)**	**Cross sec. (mm^2)**	**Heat cond (mW)**	**Heat cond. (%)**
Loading tube	1	Steel 316L	13.0	12.0	19.63	48.90	82.7
Wave guide	1	Steel 316L	5.0	4.6	3.01	7.50	12.6
CFP outer capillary	1	PEEK	3.2	2.4	3.52	0.11	0.2
CFP inner capillary	1	PEEK	1.8	1.6	0.53	0.02	0.0(*)
Coax cable shield	1	Steel 304L	3.2	3.0	0.97	2.50	4.2
New insert	**5**	**Miscellaneous**	\	\	\	**59.10**	**100**

Maximum solid-state polarization was back calculated from the liquid-state value assuming a pyruvate low field T_1 of 60 s and a time interval between end of the dissolution and beginning of the liquid-state acquisition of 7 s for the original insert and 8.5 s for the new one (see next paragraph).

2.8. Liquid-state measurements

After shining microwaves at optimal conditions for as long as 3 buildup time constants, each sample was dissolved and transferred to a 14.1 T / 26 cm horizontal bore magnet (Magnex Scientific, Oxford, United Kingdom), interfaced to a BioSpec Advance NEO spectrometer (Bruker BioSpin, Ettlingen, Germany) to measure its liquid-state polarization and relaxation time. To dissolve the samples, 5.5 mL of buffer solution (40 mM Tris in D_2O balanced to pD = 7.6) was heated to 170 – 180 °C (12 bar of vapor pressure) and pushed with helium gas over a 6 m long, 2.0/3.0 mm ID/OD PTFE tube into a separator/infusion pump placed in the isocenter of the horizontal magnet [18]. Prior to release the superheated buffer, for the old DNP insert, the dissolution procedure entailed to repressurize the sample space, to remove the waveguide, to lift the sample stick in order to raise the sample cup above the liquid He level, and finally to insert the dissolution wand to be docked on top of the sample cup [18]. For the new DNP insert, the "dissolution head" was removed from the dissolution wand and placed at a fixed position on top of the polarizer (Supplementary figure S2). In this case, the dissolution procedure simply entailed to pull the CFP upwards by 10 cm and connect it to the dissolution head (watch videos attached as Supporting Material).

Using the dissolution stick, the liquid was pushed during 3.5 s with a pressure of 6.0 bar, while the CFP required 5.0 s and 9.0 bar due to the higher flow resistance due to the smaller inner capillary.

After the transfer, the 2.5 ± 0.2 mL of HP solution was left to settle for 3.5 s inside the separator/infusion pump. Then the ^{13}C NMR signal was acquired with 10° hard pulses every 3 s for 60 times using a solenoid coil [17,33]. The decay of the HP NMR signal was fitted with a mono-exponential function to determine the ^{13}C T_1 at 14.1 T.

To measure the thermal equilibrium signal, 5 μL of 0.5 M Gd-DO3A-butrol (Gadobutrol, Gadovist, Bayer) was added to the solution collected inside the separator/infusion pump to reduce the relaxation time of pyruvate. The thermal NMR signal was acquired with 10° hard pulses, TR = 5 s and 1024 averages. The liquid-state DNP enhancement was calculated from the ratio between the HP and thermal NMR signals (n = 3 for each insert).

2.9. Statistical analysis

For each comparison metric between both DNP inserts, a one-way analysis of variance (ANOVA) in OriginPro 2019b (OriginLab, Northampton, USA) was used to compare the statistical difference between means. A p-value below 0.05 was considered significant. All values are expressed as mean ± standard deviation.

3. Results and discussion

3.1. Cryogenic performance

Fig. 4A shows the polarizer's holding time when equipped with the original DNP insert (blue line) and the new one (red line). While the old design allows to keep the sample immersed in liquid He for 4 h, the CFP design prolongs this time to 5.5 h, providing a 37.5 % improvement. An increased holding time is very advantageous when long acquisitions are required (e.g. measurement of a DNP spectrum), especially for polarizers not equipped with an automatic He filling system.

In both cases, the temperature decreases slightly as a function of time because the sample space pressure, and thus the temperature, is affected by the liquid He level inside the cryostat. Less He means less boil off, therefore a lower achievable pressure for a given pumping power. The sudden temperature drop at the end of the measurement is caused by the absence of liquid He in the cryostat. The latter is followed by a transitory drastic reduction of the pressure. Right after, the temperature rises (data not shown). Provided that the cryostat can be filled with maximum 1300 mL of liquid He, the original design boils off on average 325 mL/h, while the CFP compatible one only 236 mL/h. Therefore, the original design every hour has a liquid He consumption excess of 89 mL.

Although our model for conduction accounts for a 25 % difference in heat transfer (Fig. 4B, see Table 1 and Supporting Information for more details about the contribution of each component), this can only partially justify the prolonged holding time at 1.15 K of the new DNP insert. The original design transfers heat at a rate of 0.136 J/s, while the CFP compatible one at 0.109 J/s. The rate difference of 0.027 J/s decreases to 0.015 J/s when the cryostat is almost empty. Assuming an average consumption of 0.021 J/s, this means that the original design every hour transfers 76 J more than the new one. Therefore, only because of heat conduction, being the liquid He latent heat 21 kJ/kg and liquid He density 0.125 kg/L, the original insert boils off 30 mL of He more per hour than the CFP compatible one. This is a third of the value experimentally measured.

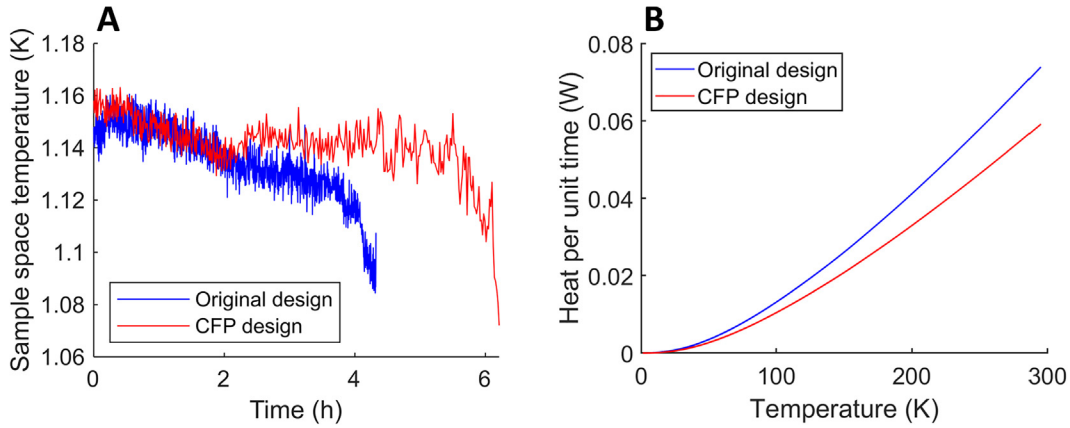

Fig. 4. **(A)** Temperature evolution as a function of time of the polarizer sample space when equipped with the original DNP insert (blue line) and the CFP compatible one (red line). (**B)** Calculation of heat transfer due to conduction for the original DNP insert (blue line) and the CFP compatible one (red line) when the cryostat is almost empty. The heat conduction difference between the two inserts is 25%. (For interpretation of the references to color in this figure legend, the reader is referred to the web version of this article.)

An explanation could be that the two designs establish different convective pathways for the boiled off He gas. In general, a laminar flow for the evaporated gas is favourable to reduce heat transfer via convection [34]. This is most likely what happens inside the new insert 12 mm ID loading tube. Differently, the original design, because of the removable waveguide and sample stick, is characterized by discontinuities in the surface of the radiation shields. These discontinuities can create turbulences in the flow of He gas and thus increased heat transfer via convection. This explanation is confirmed by the cryostat holding time measured at 4 K. At these conditions where the He boil off is less severe, the original DNP insert design allowed to keep the cryostat at 4.2 K for 15 h, while the new design for 18 h (see Supplementary Figure S7). This 20 % improvement is close to what we calculated in our heat conduction model.

In the analysis above we assumed a constant liquid He evaporation rate for the two inserts. Nevertheless, looking at Fig. 4, this is true only when the old insert is inside the cryostat. In that case, the latter boils off He at a rate of 325 mL/h, during the 4 h of holding time. Differently, when the CFP compatible insert is inside, the cryostat shows the same consumption rate for the first 2 h, and a decreased rate of 189 mL/h for the remaining 3.5 h. The rate change happens when the liquid He level drops below the 4th buffer (half of the full capacity), counting from the top (see Fig. 2). The heat conduction through the insert can justify only part of the boil-off rate. According to the simulations, this contribution ranges from 194 mL/h to 105 mL/h for the old insert, and from 155 mL/h to 84 mL/h for the new one, depending on the He level.

The other contributions come from heat conduction through the VTI and the inner wall of the cryostat, convection of the boiled off He, and radiation. A quantitative analysis of the sum of these phenomena is beyond the scope of this work. Qualitatively, we can imagine that when the He level drops, the other phenomena are attenuated, and the less efficient heat conduction of the new insert becomes more relevant. Most likely, being the last three baffles closer than the first three baffles, convection pathways are "broken" when the liquid He level drops below the 4th baffle.

In addition to the longer holding time to each He filling, the fact that the CFP compatible insert allows to exchange samples without repressurizing the polarizer sample space further reduces the He consumption during repeated experiments. Working at the system maximum capability, these improvements together allowed to save approximately 20 L of liquid He per week.

3.2. DNP spectrum and LOD-ESR results

In Fig. 5A we report the ^{13}C DNP spectrum of the sample (blue dots). [1-^{13}C]pyruvic acid doped with 20 mM of AH111501 trityl achieves its maximum polarization for a microwave frequency value of 139.86 GHz. The positive maximum DNP enhancement is slightly higher than the negative one, as already reported in previous studies for a similar sample without addition of Gd compounds [20,35,36]. The DNP spectrum nicely overlaps with the LOD-ESR one, entailing that the DNP mechanism behind is Thermal Mixing and/or Cross effect [37–40]. The latter rely on triple spin flips of one ^{13}C and two electron spins separated in energy by one nuclear Larmor frequency. Therefore, DNP can happen only for microwave frequencies where electron spins resonate. Microwave frequency modulation did not yield any further improvement implying that the spin system is optimal for direct DNP. Indeed, a trityl T_{1e} = 651 ± 10 ms is long enough, with respect to spectral diffusion, for efficient saturation of the ESR line by using monochromatic irradiation [41].

3.3. Solid-state polarization and microwave power density

Replacing the original insert with the CFP compatible one has a strong effect on the DNP performance (Fig. 6). The back calculated solid-state polarization value increases by a factor 1.52 from 24.6 ± 3.0% to 38.3 ± 1.9%. This value is in good agreement with the maximum achievable polarization (approx. 55%) that the same sample can achieve on a 5 T SPINlab, considering the different working temperature of the two machines (0.80 K vs 1.15 K). The volume normalized SNR improved by a factor 1.45. Therefore, within the experimental errors, the NMR sensitivity of the two inserts remains the same, despite the less efficient impedance matching scheme (i.e. remote tuning and matching network) of the new insert compared to the original one (i.e. local tuning and matching network) [18,33]. This behavior is due to the superior filling factor of the Alderman-Grant coil (800 μL volume) compared to the original saddle coil (3800 μL), that must accommodate the 16 mm wide sample stick. Moreover, a remote tuning and matching network is more versatile when multinuclear capability is required, being the cryogenic part of the insert the same.

The buildup time constant decreased by a factor 1.42 from 3920 ± 297 s to 2745 ± 63 s, with a standard deviation smaller by a factor 5. Most likely, the latter is due to the fixed microwave source-waveguide assembly that characterizes the new DNP insert that is not disconnected/reconnected at each dissolution/new sample loading.

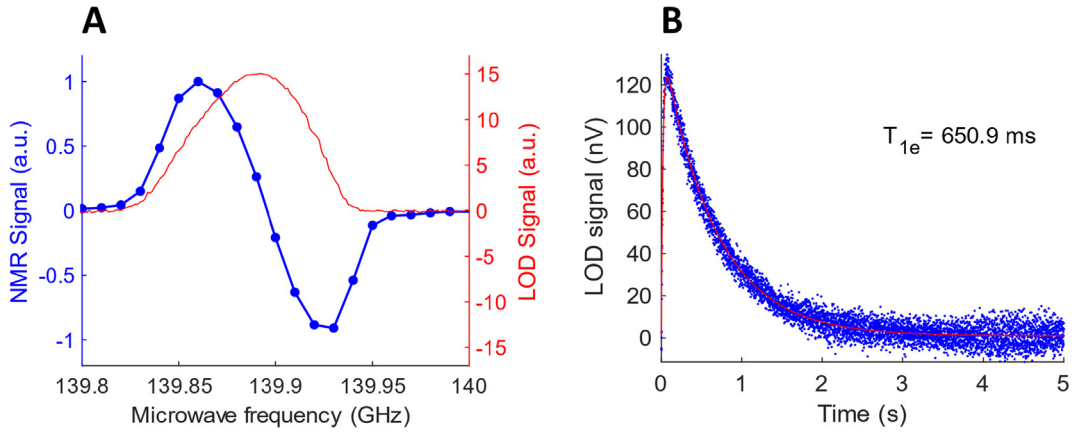

Fig. 5. [1-^{13}C]pyruvic acid NMR signal as a function of the microwave frequency (blue dots with eye-guiding line) superimposed to trityl AH111501 LOD-ESR spectrum (red line) both measured at 1.15 K and 5 T; y-axis according to color (**A**). Evolution of the radical signal as a function of time after switching off the microwaves (blue dots); the data were fitted as explained in Methods to extract the electron T_1 (red line) (**B**). (For interpretation of the references to color in this figure legend, the reader is referred to the web version of this article.)

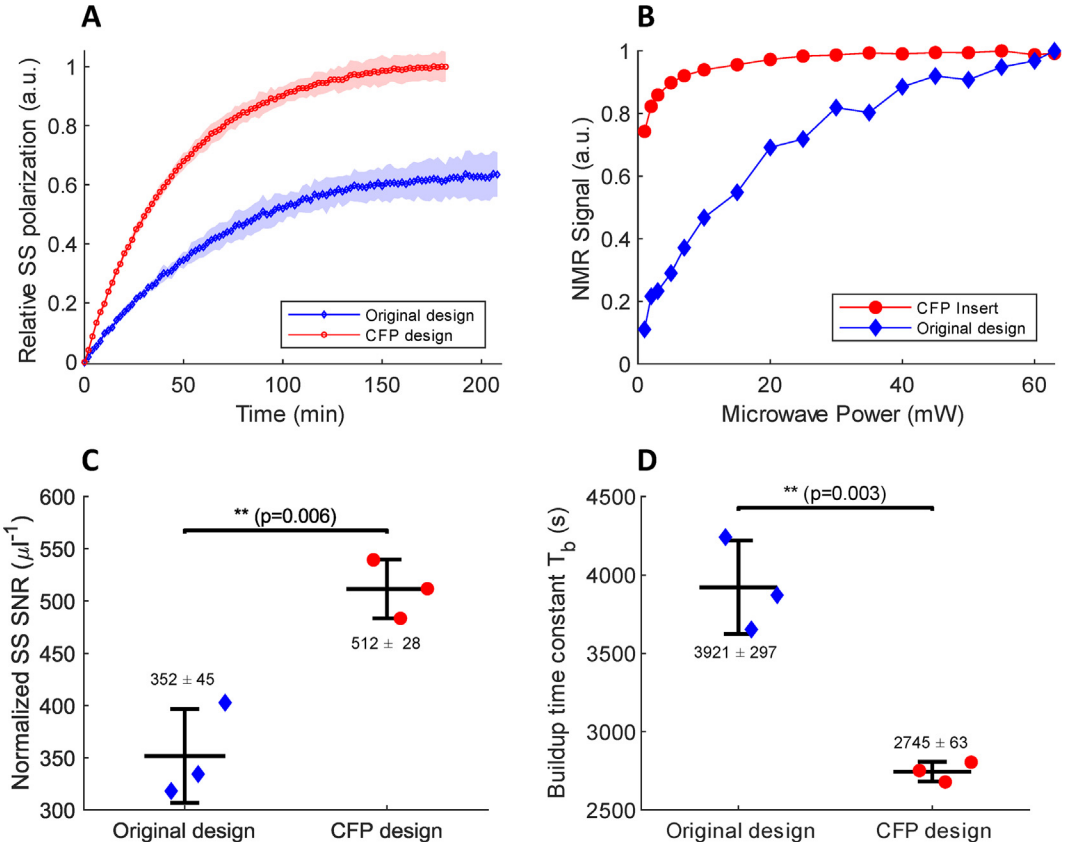

Fig. 6. Example of ^{13}C DNP solid-state build measured when shining microwaves at best conditions with original insert (blue diamonds) and the new insert (red circles); on both curves, the lighter-colored areas represent the error measured as standard deviation of three measurements. The signal intensity was normalized with respect to the highest value; the two plateaus correspond to back calculated values of 24.6 ± 3.0% to 38.3 ± 1.9% for the old and new design, respectively **(A)**. ^{13}C DNP microwave power sweep measured at 139.86 GHz when using the original insert (blue diamonds) and the new one (red dots); the lines connecting the datapoints help guiding the eyes (**B**). Sample volume normalized SNR measured in correspondence of the polarization plateau (n = 3) for the original insert (blue diamonds) and the new insert (red dots); the mean, standard deviation and p-value are reported (**C**). Build time constant resulting from the fit of polarization curves (n = 3) for the original insert (blue diamonds) and the new insert (red dots); measurements were repeated 3 times; the mean, standard deviation and p-value are reported (**D**). (For interpretation of the references to color in this figure legend, the reader is referred to the web version of this article.)

The superior polarization speed and level are a consequence of the higher microwave power density at the sample position in the new insert. Indeed, the reduced size of the microwave cavity (13.2 cm^3 vs 23.4 cm^3) allows to achieve maximum DNP enhancement already for a microwave power output of 25 mW with an onset of sample heating for 55 mW. Differently, in the original insert even at maximum output power of the microwave source (e.g. 63 mW) the DNP enhancement is still growing. This behavior is usually related to insufficient microwave power and consequent poor saturation of the radical ESR line [41,42].

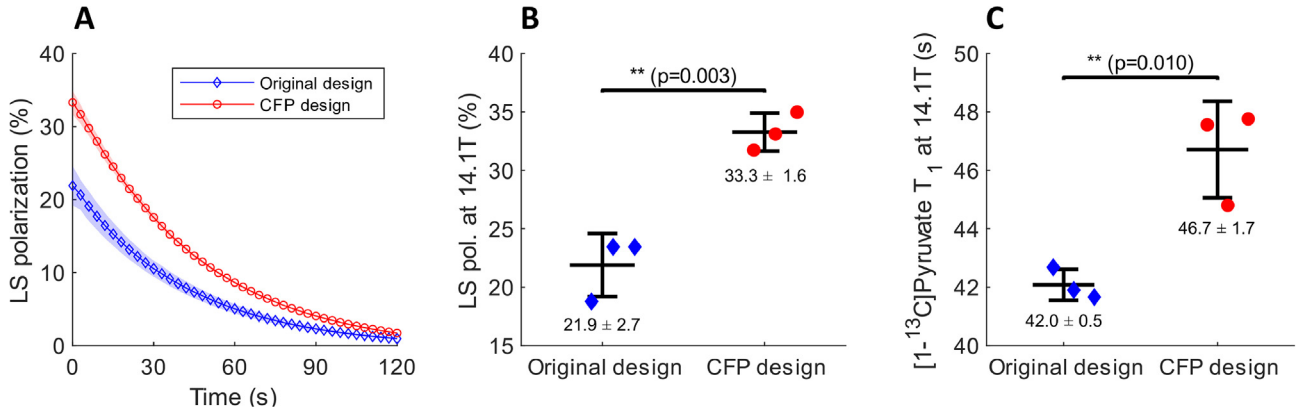

Fig. 7. Example of hyperpolarized [1-^{13}C]pyruvic acid relaxation curve measured in the 14.1 T horizontal MRI scanner after dissolution from the original insert (blue circles) and the new insert (red circles) after dissolution (**A**). Repeated measurements (n = 3) for [1-^{13}C]pyruvic acid liquid-state polarization after dissolution and pH neutralization from the original insert (blue diamonds) and the new insert (red dots); the mean, standard deviation and p-value are reported (**B**). Repeated measurements (n = 3) for [1-^{13}C] pyruvic acid liquid-state T_1 after dissolution and pH neutralization from the original insert (blue diamonds) and the new insert (red dots); the mean, standard deviation and p-value are reported (**C**). (For interpretation of the references to color in this figure legend, the reader is referred to the web version of this article.)

We would like to specify that we did not attempt to measure the sample ^{13}C NMR signal at thermal equilibrium at 5 T and 1.15 K. When trityl radical is involved, the [1-^{13}C]pyruvic acid T_1 value is several tens of hour, implying that one duly performed measurement would run over 2 or 3 days. This is costly and inconvenient in absence of an automatic liquid He filling system. The polarization values in the solid-state were back calculated from the liquid-state ones (see Methods).

3.4. Dissolution and liquid-state polarization

After dissolution and transfer, the measured liquid-state [1-^{13}C] pyruvic acid polarization increased from 21.9 ± 2.7% to 33.3 ± 1.6%, when using the CFP compatible insert (Fig. 7A and B). Despite the final ^{13}C concentration being the same (i.e. 20 mM), the T_1 increases from 42.0 ± 0.5 s to 46.7 ± 1.7 s, when dissolving the sample from the new insert (Fig. 7C). We ascribe this behavior to a temperature effect. From T_1 measurements at 14.1 T as a function of temperature of a sodium [1-^{13}C]pyruvate solution, we estimated that the relaxation time evolves as $T_1(T) = 0.877 \cdot T + 21.4$ s (see Supplementary Figure S8). Therefore, we estimate that, at the time of acquisition, the hyperpolarized solution obtained using the original insert has a temperature of 23.5 °C, while the one using the CFP insert has a temperature of 28.8 °C. These temperature values are in good agreement with the reading of a thermocouple placed inside the infusion pump/separator used to collect the hyperpolarized solution inside the bore of the MRI scanner.

Finally, it is worth stressing the fact that using a CFP dissolution system simplifies this procedure and makes it less user dependent, because it avoids any repressurization and subsequent opening of the polarizer sample space to the room environment (see videos in Supporting Material).

4. Conclusions

In this study we retrofitted a 5 T "wet" DNP polarizer. We designed, built, and tested a new DNP insert compatible with the fluid path technology. The new design allowed to increase the liquid He holding time on a single experiment from 4 h to 5.5 h and to save 20 L of liquid He during a working week. The CFP, being a sample holder and a dissolution system at the same, allowed to reduce the size of the microwave cavity. The increased microwave power density at the sample site improved the maximum achievable DNP enhancement and buildup rate constant by a factor of 1.5. This yielded, at the time of acquisition, a liquid state polarization as high as 33% on [1-^{13}C]pyruvic acid doped with trityl. Finally, the new insert can also accommodate a LOD-ESR probe for investigation of the radical properties at real DNP conditions with no need to modify/replace any part of the NMR hardware when using it.

Author contributions

Capozzi and Hyacinthe conceived the study. Lê and Capozzi designed and built the hardware. Lê performed all experiments. Capozzi built the thermodynamic model. Lê and Capozzi analyzed the data. Lê drafted the manuscript. Capozzi and Hyacinthe revised the manuscript.

Data availability

The authors declare that all data supporting the findings of this study are available within the paper and its supplementary information files. Raw data are available upon request from the corresponding author.

Funding

This work was supported by the Swiss National Science Foundation SPARK grant (CRSK-2_190547, assigned to Capozzi), the Swiss National Science Foundation Ambizione grant (PZ00P2_193276, assigned to Capozzi), the Swiss National Science Foundation Project grant (310030_170155, assigned to Hyacinthe).

Reference Data

Data available in Mendeley Data at: https://doi.org/10.17632/45jvgf589x

Declaration of Competing Interest

The authors declare that they have no known competing financial interests or personal relationships that could have appeared to influence the work reported in this paper.

Acknowledgments

The authors are grateful to Mr. Yves Pilloud and Dr. Hikari Yoshihara for their precious technical advice, and acknowledge the access to the MRI scanner of the Center for Biomedical Imaging of the Lausanne University Hospital, University of Lausanne, École polytechnique fédérale de Lausanne, University of Geneva and Geneva University Hospitals.

Appendix A. Supplementary data

Supplementary data to this article can be found online at https://doi.org/10.1016/j.jmr.2022.107197.

References

[1] A. Comment, M.E. Merritt, Hyperpolarized Magnetic Resonance as a Sensitive Detector of Metabolic Function, Biochemistry 53 (2014) 7333–7357, https://doi.org/10.1021/Bi501225t.

[2] H.-Y. Chen, R. Aggarwal, R.A. Bok, M.A. Ohliger, Z. Zhu, P. Lee, J.W. Gordon, M. van Criekinge, L. Carvajal, J.B. Slater, P.E.Z. Larson, E.J. Small, J. Kurhanewicz, D. B. Vigneron, Hyperpolarized 13C-pyruvate MRI detects real-time metabolic flux in prostate cancer metastases to bone and liver: a clinical feasibility study, Prostate Cancer Prostatic Dis 23 (2020) 269–276, https://doi.org/10.1038/s41391-019-0180-z.

[3] A. Cherubini, A. Bifone, Hyperpolarized xenon in biology, Prog. Nucl. Magn. Reson. Spectrosc. 42 (2003) 1–30, https://doi.org/10.1016/S0079-6565(02)00052-3.

[4] S. Bowen, C. Hilty, Rapid sample injection for hyperpolarized NMR spectroscopy, Phys. Chem. Chem. Phys. 12 (2010) 5766–5770, https://doi.org/10.1039/C002316g.

[5] F.A. Gallagher, R. Woitek, M.A. McLean, A.B. Gill, R. Manzano Garcia, E. Provenzano, F. Riemer, J. Kaggie, A. Chhabra, S. Ursprung, J.T. Grist, C.J. Daniels, F. Zaccagna, M.-C. Laurent, M. Locke, S. Hilborne, A. Frary, T. Torheim, C. Boursnell, A. Schiller, I. Patterson, R. Slough, B. Carmo, J. Kane, H. Biggs, E. Harrison, S.S. Deen, A. Patterson, T. Lanz, Z. Kingsbury, M. Ross, B. Basu, R. Baird, D.J. Lomas, E. Sala, J. Wason, O.M. Rueda, S.-F. Chin, I.B. Wilkinson, M.J. Graves, J.E. Abraham, F.J. Gilbert, C. Caldas, K.M. Brindle, Imaging breast cancer using hyperpolarized carbon-13 MRI, Proc. Natl. Acad. Sci. 117 (2020) 2092–2098, https://doi.org/10.1073/pnas.1913841117.

[6] L.-S. Bouchard, S.R. Burt, M.S. Anwar, K.V. Kovtunov, I.V. Koptyug, A. Pines, NMR imaging of catalytic hydrogenation in microreactors with the use of para-hydrogen, Science. 319 (2008) 442–445, https://doi.org/10.1126/science.1151787.

[7] K. Golman, O. Axelsson, H. Jóhannesson, S. Maansson, C. Olofsson, J.S. Petersson, Parahydrogen-induced polarization in imaging: Subsecond 13C angiography, Magn. Reson. Med. 46 (2001) 1–5, https://doi.org/10.1002/mrm.1152.

[8] P. Berthault, G. Huber, H. Desvaux, Biosensing using laser-polarized xenon NMR/MRI, Prog. Nucl. Magn. Reson. Spectrosc. 55 (2009) 35–60, https://doi.org/10.1016/j.pnmrs.2008.11.003.

[9] G. Duhamel, P. Choquet, E. Grillon, L. Lamalle, J.L. Leviel, A. Ziegler, A. Constantinesco, 129Xe MR imaging and spectroscopy of rat brain using arterial delivery of hyperpolarized xenon in a lipid emulsion, Magn. Reson. Med. 46 (2001) 208–212, https://doi.org/10.1002/Mrm.1180.

[10] J.H. Ardenkjær-Larsen, G.S. Boebinger, A. Comment, S. Duckett, A. Edison, F. Engelke, C. Griesinger, R.G. Griffin, C. Hilty, H. Maeda, G. Parigi, T. Prisner, E. Ravera, P.J.M. van Bentum, S. Vega, A. Webb, C. Luchinat, H. Schwalbe, L. Frydman, Facing and Overcoming Biomolecular NMR's Sensitivity Challenges, Angew Chem Int Ed (2015), https://doi.org/10.1002/anie.201410653R1.

[11] O. Szekely, G.L. Olsen, I.C. Felli, L. Frydman, High-Resolution 2D NMR of Disordered Proteins Enhanced by Hyperpolarized Water, Anal. Chem. 90 (2018) 6169–6177, https://doi.org/10.1021/acs.analchem.8b00585.

[12] A.C. Pinon, A. Capozzi, J.H. Ardenkjær-Larsen, Hyperpolarization via dissolution dynamic nuclear polarization: new technological and methodological advances, Magn. Reson. Mater. Phys. Biol. Med. 34 (2021) 5–23, https://doi.org/10.1007/s10334-020-00894-w.

[13] J.H. Ardenkjaer-Larsen, B. Fridlund, A. Gram, G. Hansson, L. Hansson, M.H. Lerche, R. Servin, M. Thaning, K. Golman, Increase in signal-to-noise ratio of > 10,000 times in liquid-state NMR, Proc. Natl. Acad. Sci. U. S. A. 100 (2003) 10158–10163, https://doi.org/10.1073/pnas.1733835100.

[14] A. Abragam, M. Goldman, Principles of Dynamic Nuclear-Polarization, Rep. Prog. Phys. 41 (1978) 395–467, https://doi.org/10.1088/0034-4885/41/3/002.

[15] J. Wolber, F. Ellner, B. Fridlund, A. Gram, H. Johannesson, G. Hansson, L.H. Hansson, M.H. Lerche, S. Maansson, R. Servin, et al., Generating highly polarized nuclear spins in solution using dynamic nuclear polarization, Nucl. Instrum. Methods Phys. Res. Sect. Accel. Spectrometers Detect. Assoc. Equip. 526 (2004) 173–181, j.nima.2004.03.171.

[16] S. Jannin, A. Comment, F. Kurdzesau, J.A. Konter, P. Hautle, B. van den Brandt, J. J. van der Klink, A 140 GHz prepolarizer for dissolution dynamic nuclear polarization, J. Chem. Phys. 128 (2008) 241102 1–4. https://doi.org/10.1063/1.2951994.

[17] T. Cheng, A. Capozzi, Y. Takado, R. Balzan, A. Comment, Over 35% liquid-state 13C polarization obtained via dissolution dynamic nuclear polarization at 7 T and 1 K using ubiquitous nitroxyl radicals, Phys. Chem. Chem. Phys. 15 (2013) 20819–20822, https://doi.org/10.1039/C3CP53022A.

[18] A. Comment, B. van den Brandt, K. Uffmann, F. Kurdzesau, S. Jannin, J.A. Konter, P. Hautle, W.T.H. Wenckebach, R. Gruetter, J.J. van der Klink, Design and performance of a DNP prepolarizer coupled to a rodent MRI scanner, Concepts Magn. Reson. Part B-Magn. Reson. Eng. 31B (2007) 255–269, https://doi.org/10.1002/Cmr.B.20099.

[19] M. Batel, M. Krajewski, K. Weiss, O. With, A. Däpp, A. Hunkeler, M. Gimersky, K. P. Pruessmann, P. Boesiger, B.H. Meier, S. Kozerke, M. Ernst, A multi-sample 94GHz dissolution dynamic-nuclear-polarization system, J. Magn. Reson. 214 (2012) 166–174, https://doi.org/10.1016/j.jmr.2011.11.002.

[20] J.-H. Ardenkjaer-Larsen, A.M. Leach, N. Clarke, J. Urbahn, D. Anderson, T.W. Skloss, Dynamic nuclear polarization polarizer for sterile use intent, NMR Biomed. 24 (2011) 927–932, https://doi.org/10.1002/nbm.1682.

[21] J.H. Ardenkjær-Larsen, S. Bowen, J.R. Petersen, O. Rybalko, M.S. Vinding, M. Ullisch, N.C. Nielsen, Cryogen-Free dissolution Dynamic Nuclear Polarization polarizer operating at 3.35 T, 6.70 T and 10.1 T., Magn. Reson. Med. 81(2019), 2184-2194, https://doi.org/10.1002/mrm.27537.

[22] M. Baudin, B. Vuichoud, A. Bornet, G. Bodenhausen, S. Jannin, A cryogen-consumption-free system for dynamic nuclear polarization at 9.4 T, J. Magn. Reson. 294 (2018) 115–121, https://doi.org/10.1016/j.jmr.2018.07.001.

[23] T. Cheng, A.P. Gaunt, I. Marco-Rius, M. Gehrung, A.P. Chen, J.J. Klink, A. Comment, A multisample 7 T dynamic nuclear polarization polarizer for preclinical hyperpolarized MR, NMR Biomed. 33 (2020), https://doi.org/10.1002/nbm.4264.

[24] A. Capozzi, J. Kilund, M. Karlsson, S. Patel, A.C. Pinon, F. Vibert, O. Ouari, M.H. Lerche, J.H. Ardenkjær-Larsen, Metabolic contrast agents produced from transported solid 13C-glucose hyperpolarized via dynamic nuclear polarization, Commun. Chem. 4 (2021) 95, https://doi.org/10.1038/s42004-021-00536-9.

[25] M. Mishkovsky, O. Gusyatiner, B. Lanz, C. Cudalbu, I. Vassallo, M.-F. Hamou, J. Bloch, A. Comment, R. Gruetter, M.E. Hegi, Hyperpolarized 13C-glucose magnetic resonance highlights reduced aerobic glycolysis in vivo in infiltrative glioblastoma, Sci. Rep. 11 (2021) 5771, https://doi.org/10.1038/s41598-021-85339-7.

[26] K. Singh, C. Jacquemmoz, P. Giraudeau, L. Frydman, J.-N. Dumez, Ultrafast 2D 1H–1H NMR spectroscopy of DNP-hyperpolarised substrates for the analysis of mixtures, Chem. Commun. 57 (2021) 8035–8038, https://doi.org/10.1039/D1CC03079E.

[27] P.R. Jensen, F. Sannelli, L.T. Stauning, S. Meier, Enhanced 13C NMR detects extended reaction networks in living cells, Chem. Commun. 57 (2021) 10572–10575, https://doi.org/10.1039/D1CC03838A.

[28] A.C. Pinon, A. Capozzi, J.H. Ardenkjær-Larsen, Hyperpolarized water through dissolution dynamic nuclear polarization with UV-generated radicals, Commun. Chem. 3 (2020) 57, https://doi.org/10.1038/s42004-020-0301-6.

[29] A. Capozzi, M. Karlsson, J.R. Petersen, M.H. Lerche, J.H. Ardenkjaer-Larsen, Liquid-State 13 C Polarization of 30% through Photoinduced Nonpersistent Radicals, J. Phys. Chem. C. 122 (2018) 7432–7443, https://doi.org/10.1021/acs.jpcc.8b01482.

[30] J. Granwehr, J. Leggett, W. Kockenberger, A low-cost implementation of EPR detection in a dissolution DNP setup, J Magn Reson. 187 (2007) 266–276, https://doi.org/10.1016/j.jmr.2007.05.011.

[31] P. Duthil, Material Properties at Low Temperature (2014), https://doi.org/10.5170/CERN-2014-005.77.

[32] Index of Material Properties, n.d. https://trc.nist.gov/cryogenics/materials/materialproperties.htm.

[33] T. Cheng, M. Mishkovsky, J.A.M. Bastiaansen, O. Ouari, P. Hautle, P. Tordo, B. van den Brandt, A. Comment, Automated transfer and injection of hyperpolarized molecules with polarization measurement prior to in vivo NMR, NMR Biomed. 26 (2013) 1582–1588, https://doi.org/10.1002/nbm.2993.

[34] J.G. Weisend II, ed., Cryostat Design: Case Studies, Principles and Engineering, 1st ed. 2016, Springer International Publishing : Imprint: Springer, Cham, 2016. https://doi.org/10.1007/978-3-319-31150-0.

[35] A. Capozzi, S. Patel, W.T. Wenckebach, M. Karlsson, M.H. Lerche, J.H. Ardenkjær-Larsen, Gadolinium Effect at High-Magnetic-Field DNP: 70% 13C Polarization of [U-13C] Glucose Using Trityl, J. Phys. Chem. Lett. 10 (2019) 3420–3425, https://doi.org/10.1021/acs.jpclett.9b01306.

[36] L. Lumata, M.E. Merritt, C.R. Malloy, A.D. Sherry, Z. Kovacs, Impact of Gd3+ on DNP of [1-13C] pyruvate doped with trityl OX063, BDPA, or 4-oxo-TEMPO, J. Phys. Chem. A. 116 (2012) 5129–5138, https://doi.org/10.1021/jp302399f.

[37] W.Th. Wenckebach, Dynamic nuclear polarization via the cross effect and thermal mixing: B. Energy transport, J. Magn. Reson. 299 (2019) 151–167, https://doi.org/10.1016/j.jmr.2018.12.020.

[38] W.Th. Wenckebach, Dynamic nuclear polarization via the cross effect and thermal mixing: A. The role of triple spin flips, J. Magn. Reson. 299 (2019) 124–134, https://doi.org/10.1016/j.jmr.2018.12.018.

[39] A. Radaelli, H.A.I. Yoshihara, H. Nonaka, S. Sando, J.H. Ardenkjaer-Larsen, R. Gruetter, A. Capozzi, 13C Dynamic Nuclear Polarization using SA-BDPA at 6.7 T and 1.1 K: Coexistence of Pure Thermal Mixing and Well-Resolved Solid Effect, J. Phys. Chem. Lett. 11 (2020) 6873–6879, https://doi.org/10.1021/acs.jpclett.0c01473.

[40] W.T. Wenckebach, A. Capozzi, S. Patel, J.H. Ardenkjær-Larsen, Direct measurement of the triple spin flip rate in dynamic nuclear polarization, J. Magn. Reson. 327 (2021), https://doi.org/10.1016/j.jmr.2021.106982.

[41] W.T. Wenckebach, Spectral diffusion and dynamic nuclear polarization: Beyond the high temperature approximation, J. Magn. Reson. 284 (2017) 104–114, https://doi.org/10.1016/j.jmr.2017.10.001.

[42] S. Jannin, A. Comment, J.J. van der Klink, Dynamic Nuclear Polarization by Thermal Mixing Under Partial Saturation, Appl. Magn. Reson. 43 (2012) 59–68, https://doi.org/10.1007/s00723-012-0363-4.